Extraction of dihadron-jet correlations with rigorous flow-background subtraction in a multiphase transport model

Yuhui Zhu(朱逾卉),[1,2] Y. G. Ma(马余刚),[1,*] J. H. Chen(陈金辉),[1] G. L. Ma(马国亮),[1] S. Zhang(张松),[1] and C. Zhong(钟晨)[1]
[1]*Shanghai Institute of Applied Physics, Chinese Academy of Sciences, Shanghai 201800, China*
[2]*University of Chinese Academy of Sciences, Beijing 100049, China*
(Received 15 May 2012; revised manuscript received 8 January 2013; published 13 February 2013)

Dihadron azimuthal correlations in Au + Au collisions at $\sqrt{S_{NN}} = 200$ GeV are explored by using a multiphase transport model. To obtain the contributions from jet-medium interactions, the combined harmonic flow background is subtracted from the raw dihadron correlation functions. The signals are compared in three associated transverse momentum ($p_T^{\rm assoc}$) bins: 0.2–0.8, 0.8–1.4, and 1.4–2.0 GeV/c from central to semiperipheral geometries. The medium modifications are observed from changes in the signal shape and the relative jet contribution is obtained within the change in the centrality from the peripheral to the central one. A strong $p_T^{\rm assoc}$ dependence of the rms width of the jet-correlation function is observed within the central geometry bin, i.e., 0–10%.

DOI: 10.1103/PhysRevC.87.024904 PACS number(s): 25.75.Gz, 12.38.Mh, 24.85.+p

I. INTRODUCTION

Lattice quantum chromodynamics (QCD) calculations predicted a phase transition from hadron gas to a deconfined matter in ultrarelativistic heavy-ion collisions [1,2]. A hot and dense partonic matter, called quark-gluon plasma (QGP), is formed in these collisions and is found to be strongly interacting.

In the literature, jet quenching [3] was used as a signal of the QGP phase formation because it is interpreted as evidence for the interaction between jets and the QGP medium. Dihadron azimuthal correlation acts as a probe for the study of jet quenching in high-energy heavy-ion collisions. During the study of dihadron azimuthal correlation functions, an away-side double-peak structure is observed in Relativistic Heavy Ion Collider (RHIC) experiments at relatively high transverse momentum (p_T) [4–6], which is regarded as evidence for jet quenching.

There are ongoing efforts within the RHIC community to study the inner mechanism of the jet-medium interaction through the dihadron correlation function. In this context, many theoretical models have been put forward over time such as the shock wave model [7], the gluon radiation model [8], medium-induced gluon bremsstrahlung [9,10], waking the colored plasma and sonic Mach cones [11], sonic booms and diffusion wakes in thermal gauge-string duality [12], jet deflection [13], and strong parton cascade mechanism [14–18].

From the above studies, we know that the dihadron azimuthal correlation signal is the key to a solid physical interpretation. However, constructing a precise dihadron correlation background is a complex task. This is mainly because of the contributions from the odd-order harmonic flows, which are induced by initial geometry fluctuations, to the away-side double-peak structure [19,20]. Theoretically, one can extract the harmonic flow coefficients and then reconstruct the high-order harmonic background. However, due to the overestimation or underestimation of the nonflow contributions in our calculation method, it is hard to get an ideal flow coefficient. Therefore, more detailed analysis concerning the background construction is needed.

In this paper, we employ two different methods for calculating background, which are discussed in detail in the upcoming section. These methods are applied for the study of transverse momentum (p_T) and centrality dependencies (0–10%, 20–40% and 50–80%) of dihadron azimuthal correlation functions in 200 GeV/c Au + Au collisions. Finally, the emphasis is put on the study of jet-induced signals in different associated p_T ($p_T^{\rm assoc}$) bins from the central collisions.

The paper is organized as follows. Section II gives a brief introduction of the simulation model. Section III describes the two different analysis methods, which are used for background construction in the study of dihadron azimuthal correlation functions. The results and discussions are given in Sec. IV, which is followed by a summary in Sec. V.

II. METHODOLOGY: A MULTIPHASE TRANSPORT MODEL

A multiphase transport (AMPT) model [21] is employed for the study of dihadron azimuthal correlations. The model has four main components for describing the physical processes in relativistic heavy-ion collisions: (1) the initial conditions from the HIJING model [22], (2) partonic interactions modeled by Zhang's parton cascade (ZPC) model [23], (3) hadronization, and (4) hadronic rescattering simulated by a relativistic transport (ART) model [24]. The model works as follows. First, many excited strings initiated from HIJING are melted into partons in the string melting version of the AMPT model [25](also called the melting AMPT version). Then, a simple quark coalescence model is used to combine the partons into hadrons. However, in the default version of the AMPT model [26] (called the default AMPT version), minijet partons are recombined with their parent strings; when they

*Author to whom correspondence should be addressed: ygma@sinap.ac.cn

stop interacting, the resulting strings are converted to hadrons via the Lund string fragmentation model [27]. This indicates that the melting AMPT version undergoes a partonic phase much more than the default AMPT version. The details of the AMPT model are available in a review paper [21] and in previous works [21,25,28].

For the present study, the melting AMPT version is used to perform the simulation for 200 GeV/c Au + Au collisions. Moreover, to concentrate on partonic stage interactions, the final hadronic rescattering process is turned off as well.

III. ANALYSIS METHOD

The raw dihadron azimuthal correlations are obtained by following the experimental procedure [4,5]. In the experiments, the azimuthal correlation is established between a high-p_T particle (trigger particle) and low-p_T particles (associated particles). In the present work, the particles in the range $p_T > 2.5$ ($p_T \leqslant 2.5$) GeV/c are specified as trigger particles (associated particles). Both the trigger and the associated particles are required to be within a pseudorapidity window of $|\eta| < 1.0$. The raw signal is obtained by accumulating pairs of trigger particles and associated particles into $\Delta\phi = \phi_{\rm assoc} - \phi_{\rm trig}$ distributions in the same event.

Normally, the dihadron combinational background can be described by the formula that follows [19,20]:

$$\langle f(\Delta\phi)\rangle_e = \left\langle \frac{N^{\rm trig}N^{\rm assoc}}{2\pi}\right\rangle_e + \left\langle \frac{N^{\rm trig}N^{\rm assoc}}{2\pi} 2\sum_{n=1}^{+\infty} v_n^{\rm trig} v_n^{\rm assoc}\right\rangle_e \cos n\Delta\phi, \quad (1)$$

where the subscript e in $\langle\cdots\rangle_e$ stands for an event-averaged quantity, while quantities without subscripts are for each event.

This is the first method that is adopted in this study [20]. By applying the method, the initial geometry anisotropy v_n^r is obtained with respect to the event plane extracted from the stage before the parton cascade. This helps to exclude as much nonflow contribution as possible. The event plane angle of each harmonic order is calculated by using the following formula:

$$\Psi_n^r = \frac{1}{n}\left[\arctan\frac{\langle r^n \sin(n\phi)\rangle}{\langle r^n\cos(n\phi)\rangle} + \pi\right], \quad (2)$$

where r and ϕ are the polar coordinates of partons in the initial coordinate space. Then $v_n^{\rm assoc}$ and $v_n^{\rm trig}$ are calculated by using the formula

$$v_n^r = \langle \cos\left[n\left(\phi - \Psi_n^r\right)\right]\rangle, \quad (3)$$

where ϕ is the azimuthal angle in the final-state momentum space. Here a resolution correction for Ψ_n^r is not necessary, because the event plane resolution from parton configuration space is considered to be nearly 100%. As discussed earlier, this procedure effectively eliminates most nonflow contributions to harmonic flows [29]. From Ref. [20], we see that, even in the most central collision ($b = 0$ fm), it is better to include higher-order flow (up to fifth order) in background construction. Therefore, we have included up to fifth-order flow contribution in background reconstruction.

However, there is a crucial point that cannot be neglected at the present stage. If one multiplies $v_n^{\rm assoc}$ and $v_n^{\rm trig}$ before they are event averaged, two-particle v_n correlation can lead to a contribution to the background, whether the factorization ($\langle v_n^{\rm assoc} v_n^{\rm trig}\rangle_e = \langle v_n^{\rm assoc}\rangle_e \langle v_n^{\rm trig}\rangle_e$) is held or not. To recover from the problem, the other modified form of the formula is also put forward in the literature [30,31]. In the modified formula, systematic errors on v_n are applied using background [Eq. (1)] as the upper bound. It can be written as

$$\langle f(\Delta\phi)\rangle_e = \left\langle \frac{N^{\rm trig}N^{\rm assoc}}{2\pi}\right\rangle_e + \left\langle \frac{N^{\rm trig}N^{\rm assoc}}{2\pi}\right\rangle_e \times 2\sum_{n=1}^{+\infty}\left\langle v_n^{\rm trig}\right\rangle_e \left\langle v_n^{\rm assoc}\right\rangle_e \cos n\Delta\phi. \quad (4)$$

There are two kinds of contributions to the difference between Eqs. (1) and (4): (1) flow fluctuation and its correlation from initial geometry asymmetry and (2) nonflow and its correlation. The first kind of contribution should be included in the background, whereas the second kind should be excluded. However, neither background Eq. (1) nor background Eq. (4) can meet the demand. Background Eq. (1) is found to overestimate background by including nonflow contribution, while background Eq. (4) underestimates the background by throwing away the background from flow fluctuation and its correlation. It is worth mentioning that effort was put forward to solve the crucial problem on decomposing flow, flow fluctuation, and nonflow [32].

Although an ideal background is hard to obtain, one can use the Eqs. (1) and (4) as the upper and lower limits of the background to get a reasonable range of jet-medium contribution. Following the same method, background is reconstructed using Eqs. (1) and (4) as the upper and lower limits for dihadron background. Correspondingly, they are marked as "background Eq. (1)" and "background Eq. (4)" in the figures. The detailed values of parameters $\langle v_1^{\rm trig}\rangle$, $\langle v_1^{\rm assoc}\rangle$, and $\langle v_1^{\rm trig} v_1^{\rm assoc}\rangle$ used in these two methods of background extractions are listed in the Appendix.

From Eqs. (1) and (4), we observed that the normalization factor of the background should be $\langle \frac{N^{\rm trig}N^{\rm assoc}}{2\pi}\rangle_e$ theoretically. Another method is to use the zero-yield at minimum (ZYAM) scheme for adjusting this factor to best match the signal with experimental findings. However, we checked the results of both methods and found that the difference between the theoretical normalization factor and the ZYAM adjustment is less than 3%.

IV. RESULTS AND DISCUSSIONS

A. Two-particle azimuthal correlation in three centrality bins

Figure 1 shows the dihadron azimuthal correlations (both raw and combined harmonic background) with different centrality bins from left to right. Each panel from top to bottom displays results with different $p_T^{\rm assoc}$ bins. For better understanding, two backgrounds are drawn simultaneously.

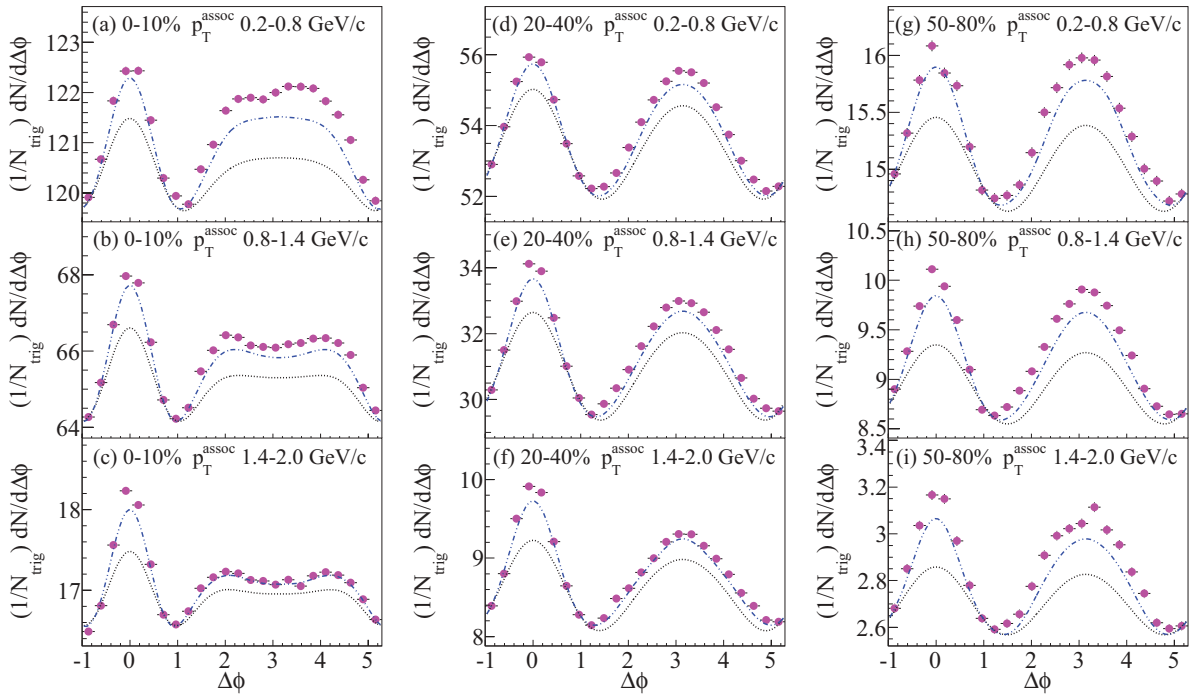

FIG. 1. (Color online) Dihadron correlation functions in 200 GeV/c Au + Au collisions derived in three p_T^{assoc} bins: (left) 0–10% centrality, (middle) 20–40% centrality, and (right) 50–80% centrality. Solid circles are raw signals. Dash-dotted blue lines are harmonic combinational backgrounds constructed using Eq. (1) and dashed black lines are backgrounds constructed using Eq. (4).

First, an obvious difference in the shape of background in different centralities is observed. The central 0–10% events have flatter or even double-peak-shaped background, while 20–40% and 50–80% ones have a single-Gaussian shape background. This is because of the different propagation properties of harmonic flows for different centralities. The existence of the hot dense matter (QGP) propagates the initial geometry irregularities to a larger extent. In Ref. [29], p_T dependencies of v_2 and v_3 show a stronger dependence especially in the large-p_T range, which makes v_3 increase more rapidly. Furthermore, the v_3 contribution is strongly affected by the change in the geometry from a central to a peripheral one. This leads to the change of combinational background shape to flatter or double peaked in the p_T range from 1.4 to 2.0 GeV/c. The two backgrounds tend to have similar shapes and just differ a little bit in magnitudes.

Second, we found a seemingly changing trend of the signal using either background. Therefore, we need to subtract the background and further study the jet-medium contribution. The corresponding plots are shown in Fig. 2. Figures 2(a)–2(c) [Figs. 2(d)–2(f)] represent the results with background Eq. (1) [Eq. (4)] subtracted. From the global comparison of these two panel sets, an obvious change in signal shape was observed. The signals in more central events (0–10%) or higher p_T^{assoc} range (e.g., 1.4–2.0 GeV/c) tend to have a flatter signal, whereas peripheral 50–80% events almost show a single-peak signal. This difference is consistent with the medium-modification picture. The existence of QGP strongly modifies jets, which makes the correlation shape flatter (or broader) in the most central collisions. In addition, it also suppresses higher-p_T particles. However, if jet interactions with surrounding medium particles are fewer (peripheral collisions), the correlation shape will tend to be single Gaussian. Moreover, the previous results indicate that there is also some contribution from hot spots when the jet production is switched off [20].

For the further analysis, a quantity named "jet relative contribution" is used to represent the contribution of the jet-medium correlation in the total dihadron correlation function. It is defined as the ratio of jet-medium correlation function yield to the raw dihadron correlation yield (including flow background). These jet relative contributions in different centrality and p_T^{assoc} bins are calculated and results are shown in Fig. 3. Figures 3(a)–3(c) are for near-side and Figs. 3(d)–3(f) are for away-side jet relative contribution. The jet relative contributions using two different backgrounds are drawn together to provide an upper and lower limit. From Fig. 3(d), one can see that the away-side jet relative contribution in central 0–10% events drops in the p_T^{assoc} range from 1.4 to 2.0 GeV/c, which is different from the case of the near-side contribution [Fig. 3(a)]. This is consistent with the high-p_T suppression picture in QGP. The quantitative values are provided in Tables I and II. In conclusion, the away-side jet relative contribution is less than 5% in central 0–10% events.

B. p_T^{assoc} dependence of jet-medium contribution in central 0–10% collisions

Since we already observed the modification to the correlation function by jet-medium interactions in Figs. 2 and 3,

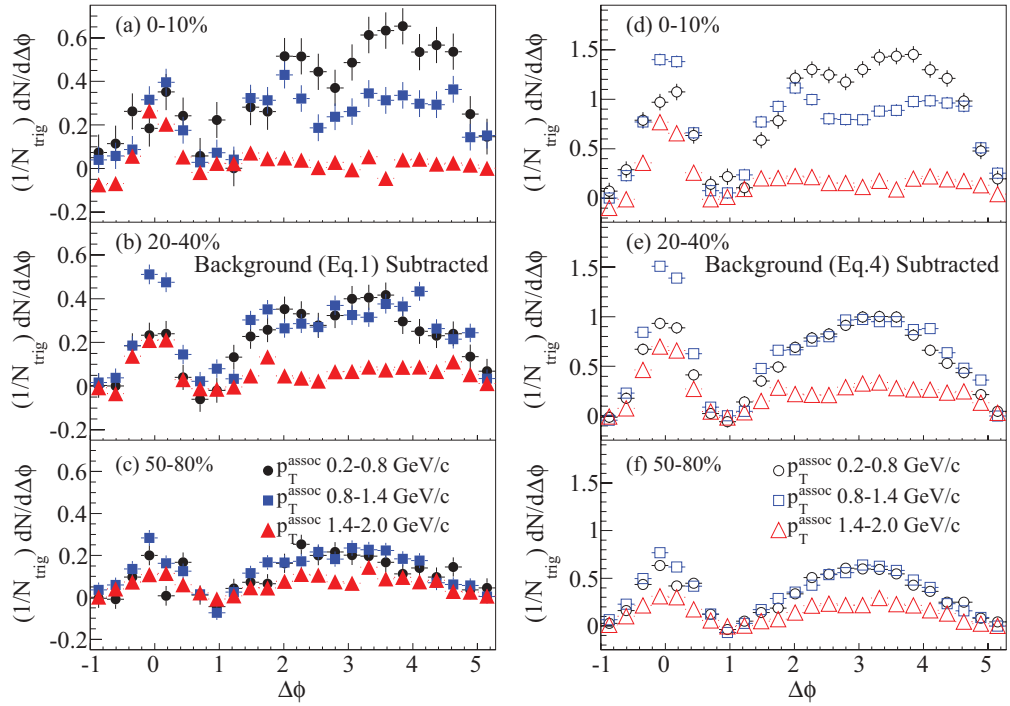

FIG. 2. (Color online) Background subtracted signals in three p_T^{assoc} bins for three centralities: (a)–(c) signals with background Eq. (1) subtracted; (d)–(f) signals after background Eq. (4) subtracted. See texts for details.

now we would like to focus on central 0–10% events for more detailed analysis. This is important because the modifications are the most obvious near the central geometry. For this purpose, the whole p_T^{assoc} range (from 0.2 to 2.4 GeV/c) is divided into much finer bins (with a bin width of 0.2 GeV/c). The results are shown in Fig. 4, where a total of 11 p_T^{assoc} bins are taken into consideration for central events. As is seen clearly from Fig. 4, the background Eq. (1) almost

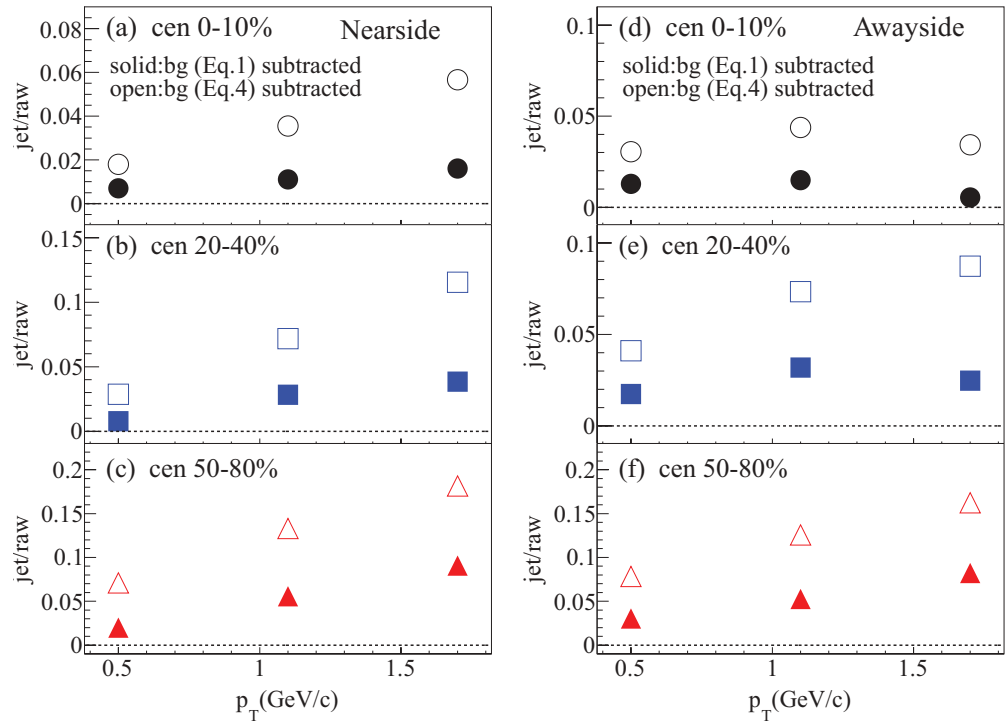

FIG. 3. (Color online) Jet relative contributions as a function of p_T^{assoc} in three centrality bins for (a)–(c) near side and (d)–(f) away side.

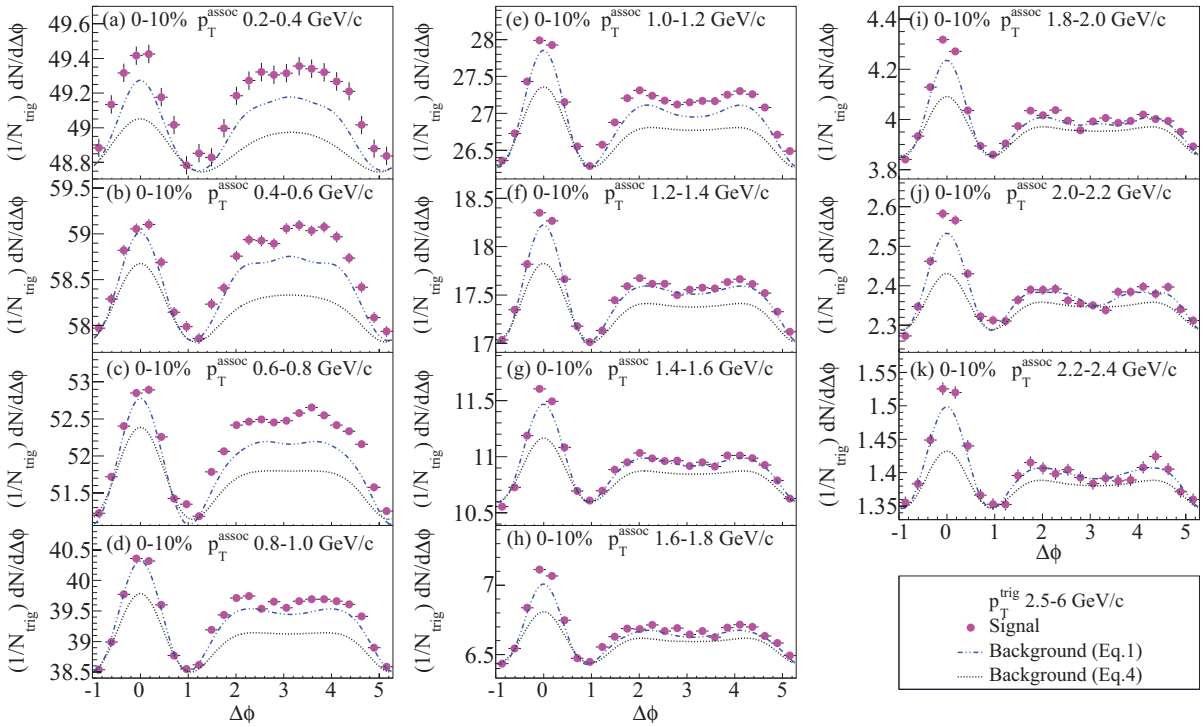

FIG. 4. (Color online) Dihadron correlation functions for different $p_T^{\rm assoc}$ bins in 200 GeV/c Au + Au collisions at 0–10% centrality. From top left to bottom right, the $p_T^{\rm assoc}$ are separated into 11 bins with 0.2 GeV/c bin width. Solid circles are raw signals, dash-dotted blue curves are the combinational background Eq. (1) cases and dotted black curves are the combinational background Eq. (4) cases.

overlaps with the raw signal in the high-p_T range (larger than 1.6 GeV/c), so we only pick out 7 p_T bin results for further analysis. For the background Eq. (4) case, all the real signals are extracted.

The extracted values of background Eq. (1) and background Eq. (4) from Fig. 4 are displayed in the left and middle panels of Fig. 5. The different colors and types of symbols represent the values extracted from different $p_T^{\rm assoc}$ bins. For the background Eq. (1) case [Figs. 5(a) and 5(b)], we found that the signal shape becomes flatter and flatter towards the high $p_T^{\rm assoc}$. For the background Eq. (4) case [Figs. 5(c)–5(e)], a clear evolution from a flat or seemingly single-peak structure to a double-peak structure with $p_T^{\rm assoc}$ is obtained. This is because of the unsubtracted v_3 fluctuation and correlation. The rms and jet relative contribution, which are extracted from the left and middle panels, are shown in Figs. 5(f) and 5(g). The $p_T^{\rm assoc}$ dependence of the rms also shows similar evolutions of away-side signal shape for both the cases. The reasonable range of jet relative contribution is shown in Fig. 5(g). These results suggest the importance of jet-medium interactions and may help elucidate the mechanisms of jet energy loss in the QGP.

V. SUMMARY

In summary, we studied the dihadron azimuthal correlation functions using a AMPT model in 200 GeV/c Au + Au collisions for different centralities of 0–10%, 20–40%, and 50–80% and different $p_T^{\rm assoc}$ bins. We obtained harmonic flows with less nonflow effect and constructed the combined harmonic flow background using two formulas as reasonable upper and lower limits. Although the backgrounds calculated by the two formulas differ in magnitude, the physics information is quite similar for both cases.

The evolution of real signal shape and away-side jet relative contribution with the increase of $p_T^{\rm assoc}$ and centrality is consistent with the fact that the high-p_T particles are strongly modified by the hot dense medium and the hot-dense-medium formation is weaker in more peripheral collisions.

TABLE I. Near-side jet-medium contribution.

	0.2–0.8 GeV/c	0.8–1.4 GeV/c	1.4–2.0 GeV/c
0–10%	0.7–1.8%	1.1–3.5%	1.6–5.7%
20–40%	0.8–2.9%	2.8–7.2%	3.8–11.5%
50–80%	2.0–7.1%	5.2–13.3%	9.1–18.1%

TABLE II. Away-side jet-medium contribution.

	0.2–0.8 GeV/c	0.8–1.4 GeV/c	1.4–2.0 GeV/c
0–10%	1.3%–3.1%	1.5%–4.4%	0.5%–3.4%
20–40%	1.7%–4.1%	3.2%–7.3%	2.5%–8.7%
50–80%	3.0%–7.8%	5.2%–12.6%	8.2%–16.2%

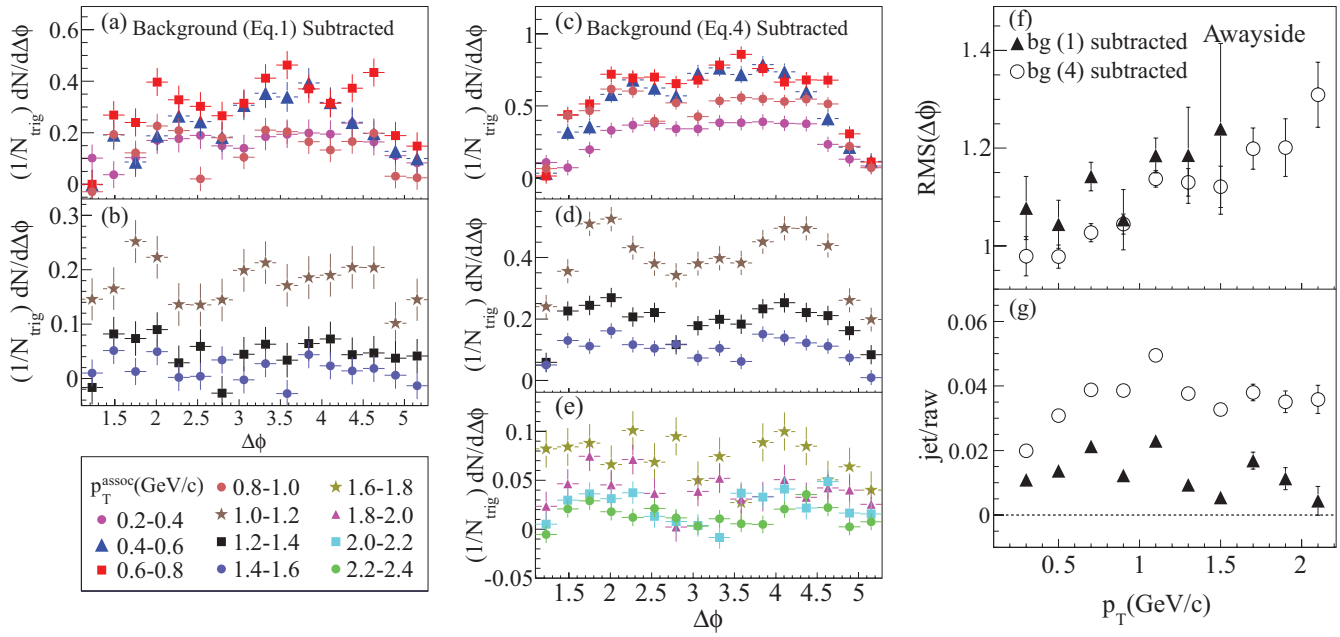

FIG. 5. (Color online) (a), (b) Background subtracted away-side signals for seven different p_T^{assoc} bins for background Eq. (1) case, (c)–(e) away-side signals for 11 different bins for background Eq. (4) case, and (f), (g) p_T^{assoc} dependencies of rms width and jet relative contribution.

The jet contribution percentage in the raw dihadron correlation function is relatively small. For the most central events (0–10%), it is less than 5%. For a reliable extraction of the jet-correlation yields, a precise understanding of the harmonic flow background to within a few percent is required. However, the jet-correlation shape is robust against a large variation in the background subtraction. We carried out a comprehensive study of jet-medium contribution as a function of p_T^{assoc} in fine bins. We observed an evolution of the correlation signal with increasing p_T^{assoc}, from a single Gaussian to a flat or even double-peaked shape. The away-side correlation function rms increases with p_T^{assoc}, even for our conservative choices of the two significantly different flow backgrounds. These results suggest the importance of jet-medium interactions and may help elucidate the mechanisms of jet energy loss in the QGP.

ACKNOWLEDGMENTS

This work was supported in part by the National Natural Science Foundation of China under Contracts No. 11035009, No. 11220101005, No. 10979074, No. 11105207, No. 11175232, and No. U1232206 and the Knowledge Innovation Project of the Chinese Academy of Sciences under Grant No. KJCX2-EW-N01.

APPENDIX: TABLES OF VALUES OF FLOW PARAMETERS

Values of various flow parameters are listed in Tables III–VIII.

TABLE III. Values of $\langle v_1^{\text{trig}} \rangle$, $\langle v_1^{\text{assoc}} \rangle$, and $\langle v_1^{\text{trig}} v_1^{\text{assoc}} \rangle$.

	0–10%			20–40%			50–80%		
p_T^{assoc} range	$\langle v_1^{\text{trig}} \rangle$	$\langle v_1^{\text{assoc}} \rangle$	$\langle v_1^{\text{trig}} v_1^{\text{assoc}} \rangle$	$\langle v_1^{\text{trig}} \rangle$	$\langle v_1^{\text{assoc}} \rangle$	$\langle v_1^{\text{trig}} v_1^{\text{assoc}} \rangle$	$\langle v_1^{\text{trig}} \rangle$	$\langle v_1^{\text{assoc}} \rangle$	$\langle v_1^{\text{trig}} v_1^{\text{assoc}} \rangle$
0.2–0.4 GeV/c	−0.025871	0.003891	−0.000697	−0.002960	0.001342	−0.000942	−0.005993	0.000993	−0.001940
0.4–0.6 GeV/c	−0.025871	0.004727	−0.001506	−0.002960	0.001394	−0.001624	−0.005993	0.000642	−0.002396
0.6–0.8 GeV/c	−0.025871	0.003769	−0.001587	−0.002960	0.001312	−0.001456	−0.005993	−0.000149	−0.002416
0.8–1.0 GeV/c	−0.025871	0.001927	−0.001085	−0.002960	0.000702	−0.001577	−0.005993	−0.000068	−0.002329
1.0–1.2 GeV/c	−0.025871	−0.000342	−0.000595	−0.002960	0.000570	−0.001468	−0.005993	0.000488	−0.003082
1.2–1.4 GeV/c	−0.025871	−0.001999	−0.000035	−0.002960	−0.000051	−0.000855	−0.005993	−0.001384	−0.003353
1.4–1.6 GeV/c	−0.025871	−0.004586	0.000807	−0.002960	−0.000390	−0.000036	−0.005993	−0.003510	−0.003151
1.6–1.8 GeV/c	−0.025871	−0.007725	0.001316	−0.002960	−0.001960	0.000864	−0.005993	0.002034	−0.003610
1.8–2.0 GeV/c	−0.025871	−0.010687	0.002172	−0.002960	−0.003233	0.001257	−0.005993	0.000679	−0.003284
2.0–2.2 GeV/c	−0.025871	−0.012145	0.003433	−0.002960	−0.002566	0.001859	−0.005993	−0.002832	−0.003654
2.2–2.4 GeV/c	−0.025871	−0.016067	0.003415	−0.002960	−0.003811	0.002671	−0.005993	−0.005312	−0.004666

TABLE IV. Values of $\langle v_2^{\rm trig}\rangle$, $\langle v_2^{\rm assoc}\rangle$, and $\langle v_2^{\rm trig} v_2^{\rm assoc}\rangle$.

	0–10%			20–40%			50–80%		
$p_T^{\rm assoc}$ range	$\langle v_2^{\rm trig}\rangle$	$\langle v_2^{\rm assoc}\rangle$	$\langle v_2^{\rm trig} v_2^{\rm assoc}\rangle$	$\langle v_2^{\rm trig}\rangle$	$\langle v_2^{\rm assoc}\rangle$	$\langle v_2^{\rm trig} v_2^{\rm assoc}\rangle$	$\langle v_2^{\rm trig}\rangle$	$\langle v_2^{\rm assoc}\rangle$	$\langle v_2^{\rm trig} v_2^{\rm assoc}\rangle$
0.2–0.4 GeV/c	0.073775	0.016994	0.001957	0.188455	0.041964	0.009125	0.164376	0.052629	0.012003
0.4–0.6 GeV/c	0.073775	0.031763	0.003030	0.188455	0.070599	0.015442	0.164376	0.081647	0.018957
0.6–0.8 GeV/c	0.073775	0.044547	0.004151	0.188455	0.095192	0.021016	0.164376	0.103296	0.024413
0.8–1.0 GeV/c	0.073775	0.053954	0.004852	0.188455	0.114463	0.025449	0.164376	0.120846	0.028254
1.0–1.2 GeV/c	0.073775	0.060495	0.005207	0.188455	0.129821	0.029124	0.164376	0.133234	0.032168
1.2–1.4 GeV/c	0.073775	0.064775	0.006021	0.188455	0.141029	0.031751	0.164376	0.143701	0.035081
1.4–1.6 GeV/c	0.073775	0.067712	0.006900	0.188455	0.149935	0.034043	0.164376	0.151426	0.038436
1.6–1.8 GeV/c	0.073775	0.068329	0.007220	0.188455	0.156176	0.035729	0.164376	0.152973	0.038768
1.8–2.0 GeV/c	0.073775	0.068417	0.007574	0.188455	0.160479	0.037796	0.164376	0.155515	0.040527
2.0–2.2 GeV/c	0.073775	0.066030	0.007593	0.188455	0.163173	0.038348	0.164376	0.159956	0.043669
2.2–2.4 GeV/c	0.073775	0.064178	0.008366	0.188455	0.163583	0.038770	0.164376	0.160305	0.043453

TABLE V. Values of $\langle v_3^{\rm trig}\rangle$, $\langle v_3^{\rm assoc}\rangle$, and $\langle v_3^{\rm trig} v_3^{\rm assoc}\rangle$.

	0–10%			20–40%			50–80%		
$p_T^{\rm assoc}$ range	$\langle v_3^{\rm trig}\rangle$	$\langle v_3^{\rm assoc}\rangle$	$\langle v_3^{\rm trig} v_3^{\rm assoc}\rangle$	$\langle v_3^{\rm trig}\rangle$	$\langle v_3^{\rm assoc}\rangle$	$\langle v_3^{\rm trig} v_3^{\rm assoc}\rangle$	$\langle v_3^{\rm trig}\rangle$	$\langle v_3^{\rm assoc}\rangle$	$\langle v_3^{\rm trig} v_3^{\rm assoc}\rangle$
0.2–0.4 GeV/c	0.100672	0.004909	0.001118	0.098937	0.010104	0.001703	0.057041	0.012910	0.002508
0.4–0.6 GeV/c	0.100672	0.015469	0.002593	0.098937	0.021127	0.003401	0.057041	0.019854	0.003226
0.6–0.8 GeV/c	0.100672	0.028102	0.004178	0.098937	0.032916	0.005453	0.057041	0.027854	0.004895
0.8–1.0 GeV/c	0.100672	0.040093	0.006086	0.098937	0.043845	0.007427	0.057041	0.033936	0.006076
1.0–1.2 GeV/c	0.100672	0.050931	0.007859	0.098937	0.053737	0.008962	0.057041	0.039496	0.006865
1.2–1.4 GeV/c	0.100672	0.059100	0.008760	0.098937	0.061137	0.010424	0.057041	0.045423	0.008008
1.4–1.6 GeV/c	0.100672	0.066054	0.009964	0.098937	0.068773	0.011919	0.057041	0.048002	0.008809
1.6–1.8 GeV/c	0.100672	0.071490	0.010496	0.098937	0.074461	0.013307	0.057041	0.051733	0.010559
1.8–2.0 GeV/c	0.100672	0.075416	0.011367	0.098937	0.077711	0.013558	0.057041	0.054062	0.010938
2.0–2.2 GeV/c	0.100672	0.076608	0.012745	0.098937	0.082178	0.014395	0.057041	0.058495	0.008238
2.2–2.4 GeV/c	0.100672	0.078378	0.013210	0.098937	0.085642	0.014619	0.057041	0.061674	0.014042

TABLE VI. Values of $\langle v_4^{\rm trig}\rangle$, $\langle v_4^{\rm assoc}\rangle$, and $\langle v_4^{\rm trig} v_4^{\rm assoc}\rangle$.

	0–10%			20–40%			50–80%		
$p_T^{\rm assoc}$ range	$\langle v_4^{\rm trig}\rangle$	$\langle v_4^{\rm assoc}\rangle$	$\langle v_4^{\rm trig} v_4^{\rm assoc}\rangle$	$\langle v_4^{\rm trig}\rangle$	$\langle v_4^{\rm assoc}\rangle$	$\langle v_4^{\rm trig} v_4^{\rm assoc}\rangle$	$\langle v_4^{\rm trig}\rangle$	$\langle v_4^{\rm assoc}\rangle$	$\langle v_4^{\rm trig} v_4^{\rm assoc}\rangle$
0.2–0.4 GeV/c	0.075574	0.000948	0.000221	0.030574	0.001625	0.000085	−0.003253	−0.001360	0.000677
0.4–0.6 GeV/c	0.075574	0.005678	0.000723	0.030574	0.004099	0.000683	−0.003253	−0.002469	0.000986
0.6–0.8 GeV/c	0.075574	0.012493	0.001632	0.030574	0.007566	0.001628	−0.003253	−0.002682	0.001783
0.8–1.0 GeV/c	0.075574	0.020305	0.002501	0.030574	0.011671	0.002133	−0.003253	−0.003266	0.002189
1.0–1.2 GeV/c	0.075574	0.028170	0.003525	0.030574	0.015414	0.003059	−0.003253	−0.002346	0.003384
1.2–1.4 GeV/c	0.075574	0.035320	0.004594	0.030574	0.018721	0.004194	−0.003253	−0.002007	0.002937
1.4–1.6 GeV/c	0.075574	0.042858	0.005170	0.030574	0.021235	0.004439	−0.003253	−0.002812	0.002656
1.6–1.8 GeV/c	0.075574	0.048819	0.005748	0.030574	0.025388	0.005695	−0.003253	−0.004228	0.001316
1.8–2.0 GeV/c	0.075574	0.053568	0.006991	0.030574	0.028373	0.006568	−0.003253	−0.005650	0.002296
2.0–2.2 GeV/c	0.075574	0.056891	0.006922	0.030574	0.029028	0.006538	−0.003253	−0.002869	0.005727
2.2–2.4 GeV/c	0.075574	0.058573	0.007499	0.030574	0.031020	0.005983	−0.003253	−0.000363	0.005555

TABLE VII. Values of $\langle v_5^{\rm trig}\rangle$, $\langle v_5^{\rm assoc}\rangle$, and $\langle v_5^{\rm trig} v_5^{\rm assoc}\rangle$.

	0–10%			20–40%			50–80%		
$p_T^{\rm assoc}$ range	$\langle v_5^{\rm trig}\rangle$	$\langle v_5^{\rm assoc}\rangle$	$\langle v_5^{\rm trig} v_5^{\rm assoc}\rangle$	$\langle v_5^{\rm trig}\rangle$	$\langle v_5^{\rm assoc}\rangle$	$\langle v_5^{\rm trig} v_5^{\rm assoc}\rangle$	$\langle v_5^{\rm trig}\rangle$	$\langle v_5^{\rm assoc}\rangle$	$\langle v_5^{\rm trig} v_5^{\rm assoc}\rangle$
0.2–0.4 GeV/c	0.035613	0.000163	0.000072	−0.004876	−0.000210	0.000189	−0.006631	−0.001752	−0.000043
0.4–0.6 GeV/c	0.035613	0.001217	0.000029	−0.004876	−0.000709	0.000279	−0.006631	−0.003521	−0.000147
0.6–0.8 GeV/c	0.035613	0.003841	0.000401	−0.004876	−0.000459	0.000549	−0.006631	−0.004073	0.000861
0.8–1.0 GeV/c	0.035613	0.006993	0.000565	−0.004876	−0.000890	0.000854	−0.006631	−0.004225	0.000594
1.0–1.2 GeV/c	0.035613	0.010640	0.001154	−0.004876	−0.000437	0.000669	−0.006631	−0.005513	−0.000439
1.2–1.4 GeV/c	0.035613	0.014408	0.001556	−0.004876	−0.000367	0.000239	−0.006631	−0.005430	0.001545
1.4–1.6 GeV/c	0.035613	0.018030	0.001783	−0.004876	0.000923	0.000809	−0.006631	−0.006749	0.001939
1.6–1.8 GeV/c	0.035613	0.020953	0.002676	−0.004876	0.002621	0.001746	−0.006631	−0.007577	0.002326
1.8–2.0 GeV/c	0.035613	0.023771	0.002333	−0.004876	0.001566	0.001071	−0.006631	−0.005370	0.001255
2.0–2.2 GeV/c	0.035613	0.027007	0.003120	−0.004876	0.001490	0.002077	−0.006631	−0.011794	0.001494
2.2–2.4 GeV/c	0.035613	0.030243	0.002670	−0.004876	0.003509	0.002326	−0.006631	−0.011982	0.001287

TABLE VIII. Values of $\langle v_6^{\rm trig}\rangle$, $\langle v_6^{\rm assoc}\rangle$, and $\langle v_6^{\rm trig} v_6^{\rm assoc}\rangle$.

	0–10%			20–40%			50–80%		
$p_T^{\rm assoc}$ range	$\langle v_6^{\rm trig}\rangle$	$\langle v_6^{\rm assoc}\rangle$	$\langle v_6^{\rm trig} v_6^{\rm assoc}\rangle$	$\langle v_6^{\rm trig}\rangle$	$\langle v_6^{\rm assoc}\rangle$	$\langle v_6^{\rm trig} v_6^{\rm assoc}\rangle$	$\langle v_6^{\rm trig}\rangle$	$\langle v_6^{\rm assoc}\rangle$	$\langle v_6^{\rm trig} v_6^{\rm assoc}\rangle$
0.2–0.4 GeV/c	0.014519	−0.000231	0.000120	−0.013741	0.000010	−0.000044	−0.001509	0.000120	−0.000396
0.4–0.6 GeV/c	0.014519	0.000030	0.000215	−0.013741	−0.000491	−0.000084	−0.001509	−0.001390	−0.000110
0.6–0.8 GeV/c	0.014519	0.000156	−0.000083	−0.013741	−0.001263	−0.000056	−0.001509	−0.001474	−0.000271
0.8–1.0 GeV/c	0.014519	0.001058	0.000036	−0.013741	−0.002195	0.000216	−0.001509	0.000550	0.000498
1.0–1.2 GeV/c	0.014519	0.002324	0.000420	−0.013741	−0.002858	0.000355	−0.001509	−0.000728	0.000465
1.2–1.4 GeV/c	0.014519	0.003721	0.000349	−0.013741	−0.003420	0.000420	−0.001509	−0.002572	−0.000688
1.4–1.6 GeV/c	0.014519	0.004106	0.000447	−0.013741	−0.003858	0.000966	−0.001509	−0.002692	0.000093
1.6–1.8 GeV/c	0.014519	0.006095	0.000886	−0.013741	−0.005499	0.000622	−0.001509	−0.002420	0.002307
1.8–2.0 GeV/c	0.014519	0.007962	0.001136	−0.013741	−0.004095	0.000763	−0.001509	−0.002748	0.001520
2.0–2.2 GeV/c	0.014519	0.007611	−0.000213	−0.013741	−0.001545	0.000804	−0.001509	0.002193	−0.000750
2.2–2.4 GeV/c	0.014519	0.008142	0.000370	−0.013741	−0.001668	0.000705	−0.001509	0.003055	0.000971

[1] F. R. Brown, F. P. Butler, Hong Chen, N. H. Christ, Zhihua Dong, W. Schaffer, L. I. Unger, and A. Vaccarino, Phys. Rev. Lett. **65**, 2491 (1990).

[2] I. Arsene *et al.*, Nucl. Phys. A **757**, 1 (2005); B. B. Back *et al.* (PHOBOS Collaboration), *ibid.* **757**, 28 (2005); J. Adams *et al.* (STAR Collaboration), *ibid.* **757**, 102 (2005); S. S. Adcox *et al.* (PHENIX Collaboration), *ibid.* **757**, 184 (2005).

[3] X.-N. Wang and M. Gyulassy, Phys. Rev. Lett. **68**, 1480 (1992).

[4] J. Adams *et al.* (STAR Collaboration), Phys. Rev. Lett. **95**, 152301 (2005).

[5] S. S. Adler *et al.* (PHENIX Collaboration), Phys. Rev. Lett. **97**, 052301 (2006).

[6] B. I. Abelev *et al.*, Phys. Rev. Lett. **102**, 052302 (2009).

[7] H. Stoecker, Nucl. Phys. A **750**, 121 (2005); J. Casalderrey-Solana *et al.*, J. Phys. Conf. Ser. **27**, 22 (2005); Nucl. Phys. A **774**, 577 (2006).

[8] V. Koch, A. Majumder, and Xin-Nian Wang, Phys. Rev. Lett. **96**, 172302 (2006).

[9] I. Vitev, Phys. Lett. B **630**, 78 (2005).

[10] A. D. Polosa and C. A. Salgado, Phys. Rev. C **75**, 041901(R) (2007).

[11] J. Ruppert and B. Müller, Phys. Lett. B **618**, 123 (2005); R. B. Neufeld, B. Muller, and J. Ruppert, Phys. Rev. C **78**, 041901 (2008).

[12] S. S. Gubser, S. S. Pufu, and A. Yarom, Phys. Rev. Lett. **100**, 012301 (2008).

[13] N. Armesto, C. A. Salgado, and U. A. Wiedemann, Phys. Rev. C **72**, 064910 (2005).

[14] Y. G. Ma, J. Phys. G **32**, S373 (2006).

[15] G. L. Ma *et al.*, Phys. Lett. B **641**, 362 (2006).

[16] G. L. Ma *et al.*, Phys. Lett. B **647**, 122 (2007).

[17] G. L. Ma, S. Zhang, Y. G. Ma, X. Z. Cai, J. H. Chen, Z. J. He, H. Z. Huang, J. L. Long, W. Q. Shen, X. H. Shi, C. Zhong, and J. X. Zuo, arXiv:nucl-th/0610088.

[18] S. Zhang *et al.*, Phys. Rev. C **76**, 014904 (2007).

[19] J. Xu and C. M. Ko, Phys. Rev. C **83**, 021903 (2011).

[20] G. L. Ma and X. N. Wang, Phys. Rev. Lett. **106**, 162301 (2011).

[21] Z. W. Lin, C. M. Ko, B. A. Li, B. Zhang, and S. Pal, Phys. Rev. C **72**, 064901 (2005).

[22] X.-N. Wang and M. Gyulassy, Phys. Rev. D **44**, 3501 (1991); M. Gyulassy and X.-N. Wang, Comput. Phys. Commun. **83**, 307 (1994).

[23] B. Zhang, Comput. Phys. Commun. **109**, 193 (1998).
[24] B. A. Li and C. M. Ko, Phys. Rev. C **52**, 2037 (1995).
[25] Z. W. Lin and C. M. Ko, Phys. Rev. C **65**, 034904 (2002); Z. W. Lin, C. M. Ko, and S. Pal, Phys. Rev. Lett. **89**, 152301 (2002).
[26] B. Zhang, C. M. Ko, B. A. Li, and Z. Lin, Phys. Rev. C **61**, 067901 (2000).
[27] B. Andersson, G. Gustafson, G. Ingelman, and T. Sjöstrand, Phys. Rep. **97**, 31 (1983).
[28] J. H. Chen *et al.*, Phys. Rev. C **74**, 064902 (2006).
[29] L. X. Han, G. L. Ma, Y. G. Ma, X. Z. Cai, J. H. Chen, S. Zhang, and C. Zhong, Phys. Rev. C **84**, 064907 (2011).
[30] M. M. Aggarwal *et al.* (STAR Collaboration), Phys. Rev. C **82**, 024912 (2010).
[31] G. Agakishiev *et al.* (STAR Collaboration), Phys. Rev. C **85**, 014903 (2012).
[32] L. Yi, F. Q. Wang, and A. H. Tang, arXiv:1101.4646; L. Xu, L. Yi, D. Kikola, J. Konzer, F. Q. Wang, and W. Xie, Phys. Rev. C **86**, 024910 (2012).